Architecture of cell–cell junctions in situ reveals a mechanism for bacterial biofilm inhibition

Charlotte E. Melia[a,b], Jani R. Bolla[c], Stefan Katharios-Lanwermeyer[d], Daniel B. Mihaylov[a,b], Patrick C. Hoffmann[e], Jiandong Huo[f,g], Michael R. Wozny[e], Louis M. Elfari[a,b], Jan Böhning[a,b], Ashleigh N. Morgan[a,b], Charlie J. Hitchman[a,b], Raymond J. Owens[f,g], Carol V. Robinson[c], George A. O'Toole[d], and Tanmay A. M. Bharat[a,b,1]

[a]Sir William Dunn School of Pathology, University of Oxford, Oxford OX1 3RE, United Kingdom; [b]Central Oxford Structural Microscopy and Imaging Centre, University of Oxford, Oxford OX1 3RE, United Kingdom; [c]Physical and Theoretical Chemistry Laboratory, University of Oxford, Oxford OX1 3TA, United Kingdom; [d]Department of Microbiology and Immunology, Geisel School of Medicine, Dartmouth College, Hanover, NH 03755; [e]Cell Biology Division, MRC Laboratory of Molecular Biology, Cambridge CB2 0QH, United Kingdom; [f]Protein Production Facility United Kingdom, Rosalind Franklin Institute - Research Complex at Harwell, Didcot OX11 0FA, United Kingdom; and [g]Division of Structural Biology, The Wellcome Centre for Human Genetics, University of Oxford, Oxford OX3 7BN, United Kingdom

Edited by E. Peter Greenberg, University of Washington, Seattle, WA, and approved June 24, 2021 (received for review June 7, 2021)

Many bacteria, including the major human pathogen *Pseudomonas aeruginosa*, are naturally found in multicellular, antibiotic-tolerant biofilm communities, in which cells are embedded in an extracellular matrix of polymeric molecules. Cell–cell interactions within *P. aeruginosa* biofilms are mediated by CdrA, a large, membrane-associated adhesin present in the extracellular matrix of biofilms, regulated by the cytoplasmic concentration of cyclic diguanylate. Here, using electron cryotomography of focused ion beam–milled specimens, we report the architecture of CdrA molecules in the extracellular matrix of *P. aeruginosa* biofilms at intact cell–cell junctions. Combining our in situ observations at cell–cell junctions with biochemistry, native mass spectrometry, and cellular imaging, we demonstrate that CdrA forms an extended structure that projects from the outer membrane to tether cells together via polysaccharide binding partners. We go on to show the functional importance of CdrA using custom single-domain antibody (nanobody) binders. Nanobodies targeting the tip of functional cell-surface CdrA molecules could be used to inhibit bacterial biofilm formation or disrupt preexisting biofilms in conjunction with bactericidal antibiotics. These results reveal a functional mechanism for cell–cell interactions within bacterial biofilms and highlight the promise of using inhibitors targeting biofilm cell–cell junctions to prevent or treat problematic, chronic bacterial infections.

biofilms | cryo-EM | in situ imaging | nanobody | antibiotics

Prokaryotic cells including bacteria and archaea are frequently found in nature as part of surface-attached, multicellular communities called biofilms (1–3). Biofilms constitute the majority of bacterial biomass on Earth (1), representing a fundamental mode of bacterial existence. While bacterial biofilms may prove beneficial to eukaryotes as host-associated microbiomes (4, 5), the formation of pathogenic bacterial biofilms is associated with the establishment of serious chronic antibiotic-tolerant infections (6).

Recently, important advances have been made in understanding early events in biofilm formation (7); however, the molecular mechanisms underlying how mature biofilms are formed and stabilized are still poorly understood. One of the hallmarks of mature biofilms is the presence of an extracellular polymeric substance (EPS) matrix that binds bacterial cells together into a sessile community, promoting antibiotic tolerance and providing protection from other predatory organisms (8–11). The EPS matrix of biofilms is a complex mixture of molecules, consisting of proteins, polysaccharides, and extracellular DNA (12). Comprehending the spatial arrangement of molecules in the EPS matrix of biofilms has been problematic (13) due to the inherent difficulty associated with high-resolution microscopic imaging inside the tissue-like environment of a biofilm. As a result, mechanisms of cellular tethering and the architecture of cell–cell junctions within biofilms are incompletely understood at the fundamental molecular level.

Nevertheless, elegant optical microscopy studies on *Vibrio cholerae* biofilms have provided clues to the internal organization of the EPS matrix, revealing that the proteins required for mature biofilm formation (RbmA, Bap1, and RbmC) fail to accumulate at the cell surface in the absence of an exopolysaccharide (called VPS) and that loss of RbmA function dramatically alters biofilm architecture (14, 15). In vitro studies of *V. cholerae* proteins have revealed an exopolysaccharide-dependent (RbmA) adhesin oligomerization pathway (16), and other studies suggest that direct interactions between the RbmA adhesin and glycans on partner cells lead to cell–cell adhesion (17). In *Escherichia coli*, an auto-aggregating adhesin known as Antigen 43 (Ag43) has been proposed to mediate cell–cell interactions in biofilms by a "Velcro-like" mechanism in which two Ag43 molecules from apposing cells dimerize to bind cells to each other (18). In both of these comparatively well-characterized bacterial species, direct visualization of the EPS matrix has thus far not been performed at the macromolecular scale, and the spatial arrangement of molecules at cell–cell junctions remains unclear.

Pseudomonas aeruginosa is a human pathogen of critical concern, posing a significant challenge in hospital settings due to its ability to form antibiotic-tolerant biofilms (19–21). Cell–cell interactions in

Significance

***Pseudomonas aeruginosa* bacteria form antibiotic-tolerant biofilms that pose significant challenges in clinical settings. Overcoming these challenges requires fundamental insights into how biofilms are formed, combined with innovative strategies to disrupt biofilms. Electron cryotomography in situ data presented here reveal the arrangement of the key *P. aeruginosa* adhesin CdrA at biofilm cell–cell junctions. Guided by our imaging data, we raised and characterized a CdrA-specific nanobody binder capable of disrupting these cell–cell junctions, thereby increasing the efficacy of antibiotic-mediated bacterial killing in biofilms. Together these data provide a pathway for developing effective alternative bacterial infection treatment strategies.**

Author contributions: C.E.M. and T.A.M.B. designed research; C.E.M., J.R.B., S.K.-L., D.B.M., P.C.H., J.H., M.R.W., L.M.E., J.B., A.N.M., C.J.H., and T.A.M.B. performed research; J.R.B., S.K.-L., P.C.H., J.H., M.R.W., L.M.E., J.B., R.J.O., C.V.R., and G.O. contributed new reagents/analytic tools; C.E.M., J.R.B., S.K.-L., D.B.M., L.M.E., J.B., R.J.O., C.V.R., G.A.O., and T.A.M.B. analyzed data; and C.E.M. and T.A.M.B. wrote the paper.

The authors declare no competing interest.

This article is a PNAS Direct Submission.

[1]To whom correspondence may be addressed. Email: tanmay.bharat@path.ox.ac.uk.

This article contains supporting information online at https://www.pnas.org/lookup/suppl/doi:10.1073/pnas.2109940118/-/DCSupplemental.

Published July 28, 2021.

the EPS matrix of *P. aeruginosa* biofilms are facilitated by the expression of a ∼220 kDa adhesin (Fig. 1*A*) known as CdrA in a cyclic diguanylate (c-di-GMP)–dependent manner (22). Under high cytoplasmic c-di-GMP concentrations, CdrA expression is increased, and the mature CdrA protein is tethered to the outer membrane of *P. aeruginosa* cells through its membrane protein partner CdrB (22, 23). In these conditions, CdrA promotes cellular aggregation and biofilm formation by directly binding to polysaccharides in the EPS matrix of biofilms, such as the Psl or Pel polysaccharides (22, 24). When cytoplasmic c-di-GMP concentrations are lower, CdrA is cleaved and released into the extracellular milieu by the action of a periplasmic protease, promoting biofilm disaggregation (22).

In this study, we have performed electron cryotomography (cryo-ET) of focused ion beam (FIB)–milled tissue-like multicellular specimens to image intact cell–cell junctions of *P. aeruginosa* bacteria, revealing the arrangement of CdrA in the extracellular matrix of *P. aeruginosa* biofilms. We have supplemented our in situ imaging with electron cryomicroscopy (cryo-EM) and native mass spectrometry (MS) experiments on biochemically purified CdrA protein, which together show that CdrA forms an extended structure at the outer membrane, forming cell–cell junctions via polysaccharide binding partners. Finally, single-domain antibodies (nanobodies) raised against purified CdrA protein provided a valuable probe to test and verify all our hypotheses experimentally on wild-type bacterial biofilms and were found to limit wild-type biofilm formation and potentiate the activity of antibiotics against mature biofilms. These data identify CdrA as a promising candidate for the development of therapeutics.

Results

CdrA Forms an Extended Structure on the Outer Membrane of *P. aeruginosa* Bacteria. To study the molecular mechanism by which CdrA tethers cells to the EPS matrix within biofilms of *P. aeruginosa*, we employed an inducible expression system in which both CdrA and CdrB are expressed. A mutation in the carboxyl-terminal part of CdrA (in the sequence TAAG, described in ref. 23) prevents the cleavage and release of CdrA into the extracellular environment, locking the protein in a biofilm-promoting state. Upon expression of the biofilm-promoting CdrA adhesin and its membrane anchor CdrB, *P. aeruginosa* cells formed biofilm-like floccules in solution (*SI Appendix*, Fig. S1*A*). Floccules formed by a Δ*psl* strain that lacked the Psl polysaccharide were smaller than in the corresponding wild-type PAO1 strain and could be disrupted by vigorous agitation alone. Floccules formed by wild-type PAO1 were extensively stained by a mannose-sensitive lectin, unlike the corresponding Δ*psl* strain (Fig. 1*B*), and could only be fully disrupted by agitation when the medium was supplemented with an excess of D-mannose sugar (Fig. 1*C* and *SI Appendix*, Fig. S1*B*), demonstrating that cell–cell clumping mediated by CdrAB is polysaccharide-dependent in wild-type PAO1 *P. aeruginosa*, confirming previous reports (22, 24). Cryo-ET of single cells expressing CdrAB, disassembled from cell clumps by vigorous

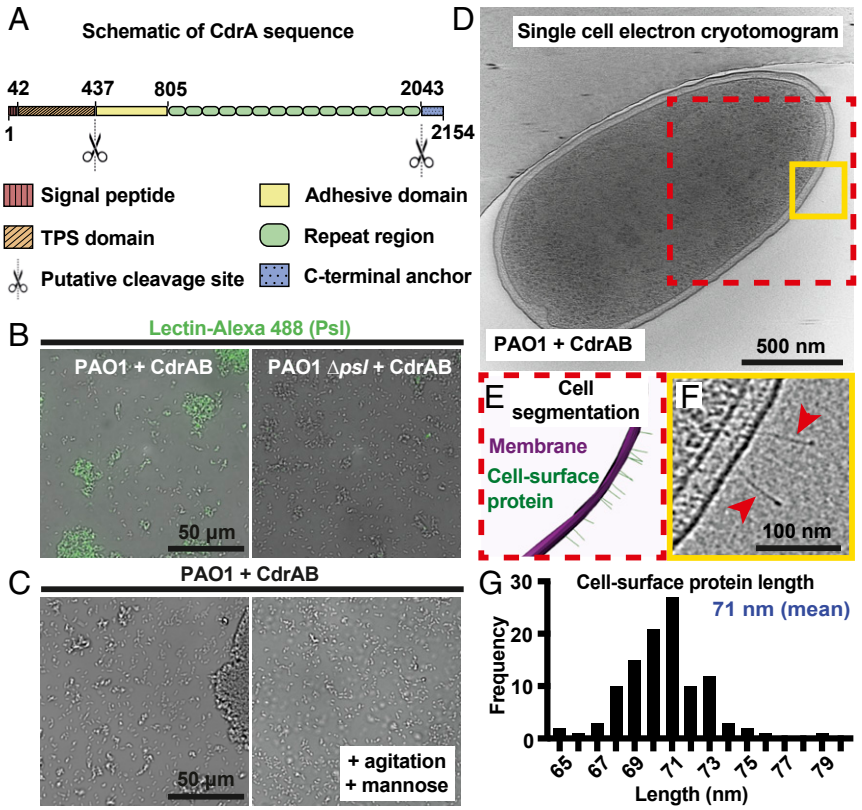

Fig. 1. CdrAB expression results in the appearance of ∼70-nm-long, matchstick-shaped protrusions on the surface of *P. aeruginosa* cells. (*A*) Schematic representation of the CdrA sequence highlighting previously determined and predicted functional regions including a TPS (two-partner secretion) domain, putative N-terminal cleavage site, and the known carboxyl-terminal cleavage site. (*B*) PAO1 (*Left*) and PAO1 Δ*psl* (*Right*) induced to express CdrAB and stained with fluorescent (Alexa 488) lectin to label mannose-containing polysaccharides. (*C*) Floccules formed by CdrAB expression before (*Left*) and after agitation in the presence of mannose (*Right*). (*D*) A slice through an electron cryotomogram of a *P. aeruginosa* PAO1 cell expressing CdrAB. (*E*) Three-dimensional segmentation of the boxed area in *D* (red dashed line). The outer membrane of the cell (purple) and matchstick-shaped cell surface molecules (green) are shown. (*F*) Cropped and magnified view of the boxed region from the tomographic slice shown in *D* (solid yellow line) with matchstick-shaped protrusions indicated (red arrowheads). (*G*) Length quantification of cell-surface matchstick-shaped protrusions; lengths are measured in electron cryotomograms (71 ± 2 nm [SD, n = 108] from 12 tomograms). Refer also to *SI Appendix*, Fig. S1 and Movie S1.

vortexing in the presence of excess D-mannose, showed protrusions emanating from the *P. aeruginosa* cell surface (Fig. 1 *D–F* and *SI Appendix*, Fig. S1 *C–E* and Movie S1). These ∼3-nm-wide protrusions projected roughly orthogonally to the outer membrane of *P. aeruginosa* and had a broad tip, resulting in a matchstick-like appearance. The length of these matchstick-shaped protrusions was 71 ± 2 nm (SD, $n = 108$), as measured in three-dimensional cryo-ET data (Fig. 1*G*).

To establish the identity of the matchstick-shaped protrusions, molecules in the outer membrane of *P. aeruginosa* cells from the inducible CdrAB expression strain were stripped and biochemically purified (*Materials and Methods* and *SI Appendix*, Fig. S2). The major component from the purification revealed a protein running at ∼150 kDa as a single band on a gel (Fig. 2 *A*, *Inset* and *SI Appendix*, Fig. S2*A*). Proteomic peptide fingerprinting analysis of the purified sample confirmed its identity as CdrA (*SI Appendix*, Fig. S2*B*). Next, cryo-EM of the MS-verified, purified CdrA specimen revealed matchstick-shaped filamentous particles on the grid (Fig. 2*A* and Movie S2). A visual inspection of these particles suggested that they closely resembled the matchstick-shaped protrusions observed in whole-cell cryo-ET (Fig. 1 *D–F*). To probe this further, cryo-ET data of the purified sample was collected and quantified, showing that the matchstick-shaped protrusions were 71 ± 1-nm (SD, $n = 75$) long (Fig. 2*B*), again indicating that they corresponded to the same cryo-EM density observed on the *P. aeruginosa* cell surface (Fig. 1 *D–G*). To assess whether the carboxyl-terminal TRRG mutation alters the architecture of CdrA, we purified particles secreted by cells expressing wild-type CdrA (Fig. 2*C*) and found that native CdrA, in the same manner as the mutant, forms elongated matchstick-shaped particles, while no protein was detected in the uninduced control (Fig. 2*C*).

To determine the oligomerization state of CdrA in solution, the purified CdrA (TRRG mutant) protein was analyzed using native MS (*SI Appendix*, Fig. S2*C*), which showed that CdrA exists as monomers in solution. Thus, the matchstick-shaped densities observed in our cryo-ET data (Fig. 1 *D–F*) correspond to a single copy of CdrA protein projecting from the outer membrane into the extracellular environment. The measured masses of CdrA (163,286 ± 3 Da and 164,047 ± 1 Da) determined by native MS agree with previous work showing that the protein undergoes proteolytic processing into a mature functional form (22, 23).

Nanobody-Targetable CdrA Molecules Mediate Cell–Cell Interactions between *P. aeruginosa* Bacteria. We next wished to understand how CdrA mediates cell–cell interactions within the extracellular matrix of *P. aeruginosa* biofilms by direct visualization of cell–cell junctions using high-resolution cryo-ET. We used the inducible CdrAB expression strain to promote flocculation of *P. aeruginosa* cells (*SI Appendix*, Fig. S1) and deposited these floccules onto cryo-EM grids. While *P. aeruginosa* cells at the edges of the cell clump could be observed (Fig. 3*A*), the multicellular, tissue-like specimen was too thick for direct cryo-EM imaging. To visualize the internal arrangement of the cell–cell junctions, thin lamellae of these specimens were produced by cryo-FIB milling (*SI Appendix*, Fig. S3 *A* and *B*), which supported high-resolution imaging using cryo-ET.

In electron cryotomograms of cryo-FIB–milled lamellae, we observed *P. aeruginosa* bacterial cells in close proximity with each other (Fig. 3 *B* and *C*). A visual inspection of the cell–cell junctions between the *P. aeruginosa* cells revealed matchstick-shaped protrusions corresponding to CdrA molecules (Fig. 4 *A* and *B* and *SI Appendix*, Fig. S3*C*). These CdrA molecules were projecting outward, away from the bacterial outer membrane and extending between *P. aeruginosa* cells into the intercellular space (Fig. 4*C* and Movie S3). The length of these CdrA molecules was 71 ± 1 nm (SD, $n = 20$), in line with the observations of CdrA on single *P. aeruginosa* cells and also of CdrA molecules after purification (Figs. 1, 2, and 4 *D* and *E* and Movie S4). While CdrA has been shown to self-interact in the absence of polysaccharides (25), in our data, direct CdrA:CdrA linkages were never observed, nor was a "Velcro-like" side-by-side configuration of CdrA molecules from apposing cells seen. The lack of direct CdrA stacking, in conjunction with the known interactions between CdrA and polysaccharides (22, 24), and the ability of the monosaccharide mannose to disrupt CdrA-mediated cell clumps (Fig. 1*C* and *SI Appendix*, Fig. S1*B*) are all consistent with a scenario in which CdrA molecules extend out of the bacterial cell surface to tether cells through interactions with polysaccharide binding partners known to be abundant in the EPS matrix.

To assess whether these CdrA-mediated cell–cell junctions might be specifically targeted, we made use of single-domain llama antibodies (or nanobodies), which have recently been shown to be a powerful tool for structural and cell biology (26). A panel of nanobodies was raised against purified CdrA protein, and based on the ability of the nanobodies to interfere with flocculation of *P. aeruginosa* bacteria in our inducible expression system (*SI Appendix*, Fig. S1*A*, further discussed in *SI Appendix*, Fig. S5), one positive nanobody binder was selected for further experiments. This nanobody (termed NB_{CdrA}) was coupled with 5-nm gold nanoparticles (NB_{CdrA}-gold) and incubated with *P. aeruginosa* cells expressing CdrA localized to the cell surface. NB_{CdrA}-gold labeling of these cells

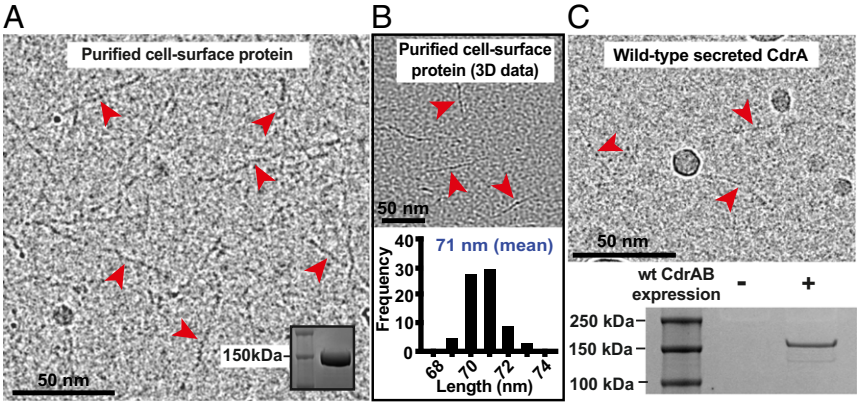

Fig. 2. Cell-surface matchstick-shaped protrusions correspond to a mature form of CdrA. (*A*) Cryo-EM micrograph of protein purified from the surface of cells expressing CdrAB. Structures resembling matchstick-shaped protrusions are indicated (red arrowheads). (*Inset*) SDS-PAGE of the purified protein. (*B*) Length quantification of purified protein resembling matchstick-shaped protrusions, measured in electron cryotomograms (71 ± 1 nm [SD, $n = 75$] from five tomograms). Refer also to *SI Appendix*, Fig. S2 and Movie S2. (*C*) Cryo-EM micrograph of protein purified from the surface of cells expressing wild-type CdrAB. Matchstick-shaped structures are indicated (red arrowheads). (*Lower*) SDS-PAGE of purified wild-type CdrA protein from an induced Δ*cdrA*/pCdrAB strain (+) versus an uninduced Δ*cdrA*/pCdrAB control (–).

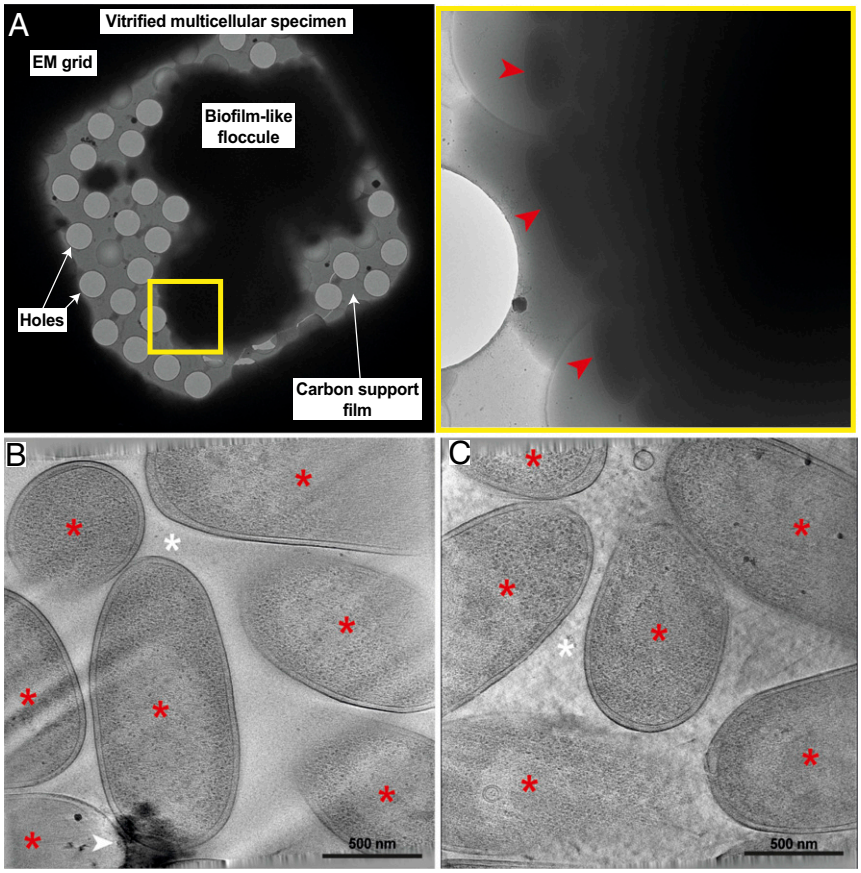

Fig. 3. FIB milling and cryo-ET of *P. aeruginosa* cell–cell junctions. (*A*) Cryo-EM of biofilm-like floccules produced by *P. aeruginosa* cells expressing CdrAB. Cryo-EM views of the multicellular aggregate. Red arrowheads indicate cells observed at the edge of the cellular aggregate (yellow box). (*B* and *C*) Cryo-ET slices through FIB-milled specimens revealing cells (red asterisks) and cell–cell junctions (white asterisks). For clarity, white arrowheads indicate ice contamination. Refer also to *SI Appendix*, Fig. S3.

revealed a shell of gold particles specifically around cells expressing CdrAB, ~70 nm from the cell surface (Fig. 5*A*). No specific NB_{CdrA}-gold labeling was observed in control cells in which CdrA was absent from the outer membrane (Fig. 5*B*), confirming that the cell-surface 71-nm matchstick-shaped protrusions correspond to CdrA molecules.

As a further verification, we performed native MS of a sample containing both purified CdrA and NB_{CdrA} and observed the formation of a 1:1 complex (Fig. 5*C*). To probe nanobody-binding, we performed a series of native MS experiments with a constant CdrA concentration titrated against increasing NB_{CdrA} concentrations. These native experiments were used to estimate a binding affinity of NB_{CdrA} with CdrA of 0.75 ± 0.26 μM (SD) (Fig. 5*D* and *SI Appendix*, Fig. S4 *A* and *B*). These binding experiments in native MS validated our microscopic observation of NB_{CdrA}-gold binding to CdrA on cells (Fig. 5 *A* and *B*). Furthermore, the 1:1 binding observed in MS, together with the localization of NB_{CdrA}-gold ~70 nm from the outer membrane, strongly suggest that a region at the broad N-terminal tip of cell-surface CdrA is specifically targeted by NB_{CdrA}.

The Anti-CdrA Nanobody Inhibits Biofilm Formation and Disrupts Preformed, Mature Biofilms. Given the mechanistic scenario suggested by our cellular (Fig. 1), in vitro (Fig. 2), and in situ imaging (Figs. 3 and 4) in which CdrA extends into and likely tethers cells to the EPS matrix, we next set out to determine whether this function of CdrA could be blocked by the targeted use of nanobodies to inhibit *P. aeruginosa* biofilm formation. First, we assessed whether the anti-CdrA nanobody (NB_{CdrA}), the nanobody shown to bind to the broad tip of CdrA molecules (Fig. 5 *A* and *B*), could disrupt CdrA-mediated cell–cell adhesion and flocculation of *P. aeruginosa* in our inducible CdrAB expression system. In line with our expectation, the addition of NB_{CdrA} disrupted preformed cell clumps, causing the cells to return to a planktonic state, forming a cloudy culture (*SI Appendix*, Fig. S5*A*). This effect could be quantified by measuring the mass of cell clumps, which confirmed that cellular aggregation decreased with increasing NB_{CdrA} concentration. In contrast, another CdrA nanobody found in our screen ($NB_{CdrA\text{-}2}$) had no effect on CdrAB-mediated flocculation (*SI Appendix*, Fig. S5*A*), potentially due to its lower binding affinity for CdrA (*SI Appendix*, Fig. S5 *B–D*). These observations suggest that a specific region at the tip of CdrA molecules ~70 nm away from the cell (as indicated by NB_{CdrA}-gold labeling) is critical for CdrA-mediated cell–cell tethering, and blocking this region with NB_{CdrA} leads to disruption of cell–cell junctions.

To explore the effect of the nanobodies on wild-type *P. aeruginosa* bacteria, a custom microfluidics flow system was used to cultivate *P. aeruginosa* biofilms. Combining the flow system with continuous fluorescence microscopy imaging, we found that the formation of *P. aeruginosa* PA14 biofilms was significantly delayed upon the addition of NB_{CdrA} (Fig. 6), showing that NB_{CdrA} can also interfere with the function of native CdrA molecules on wild-type cells. These biofilm inhibitory effects were not observed with $NB_{CdrA\text{-}2}$ (*SI Appendix*, Fig. S5*E*), confirming that $NB_{CdrA\text{-}2}$ does not interfere with the adhesive function of CdrA in the EPS matrix and demonstrating

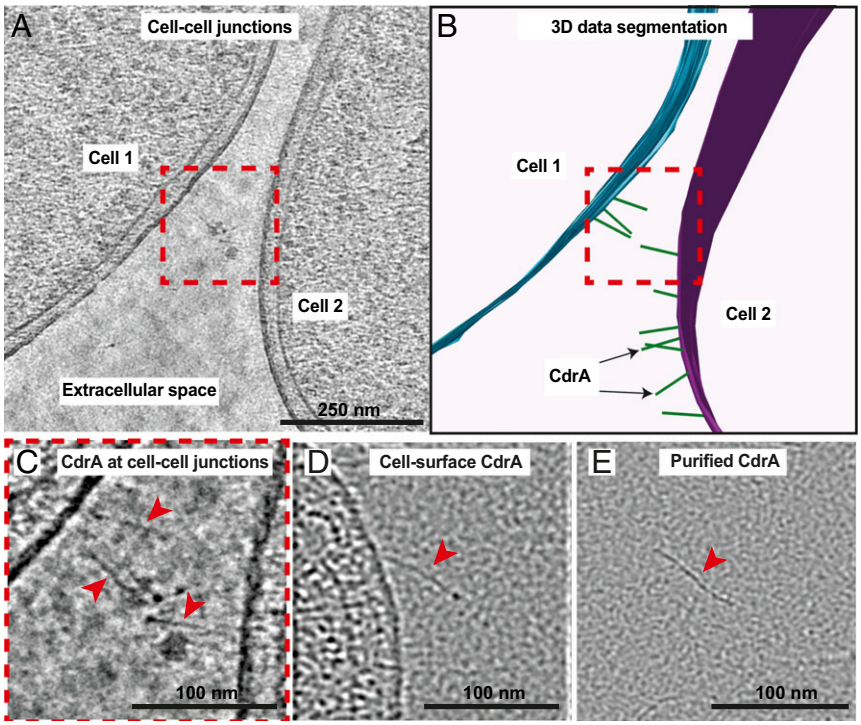

Fig. 4. CdrA extends into the EPS matrix to mediate cell–cell interactions. (*A* and *B*) Cryo-ET slice (*A*) and corresponding three-dimensional segmentation (*B*) of a cell–cell junction within a *P. aeruginosa* PAO1 biofilm-like floccule. The multicellular specimen was processed by cryo-FIB–milling into thin lamellae suitable for high-resolution cryo-ET. Cell outer membranes (blue and purple) and CdrA (green) are highlighted in *B*. (*C*) Enlarged view of the boxed region in *A*. Comparison of CdrA at cell–cell junctions within biofilm-like floccules to (*D*) CdrA on the surface of single cells and (*E*) biochemically purified CdrA in solution. CdrA is highlighted with red arrowheads. Refer also to *SI Appendix*, Fig. S3 and Movies S3 and S4.

again that targeted binding of NB_{CdrA} to the tip of functional CdrA is sufficient to inhibit biofilm formation in wild-type *P. aeruginosa* bacteria.

NB_{CdrA} access to cell-surface CdrA is likely to be greater in immature, developing biofilms in which cell–cell junctions have not yet formed and in which diffusion deep into a multicellular

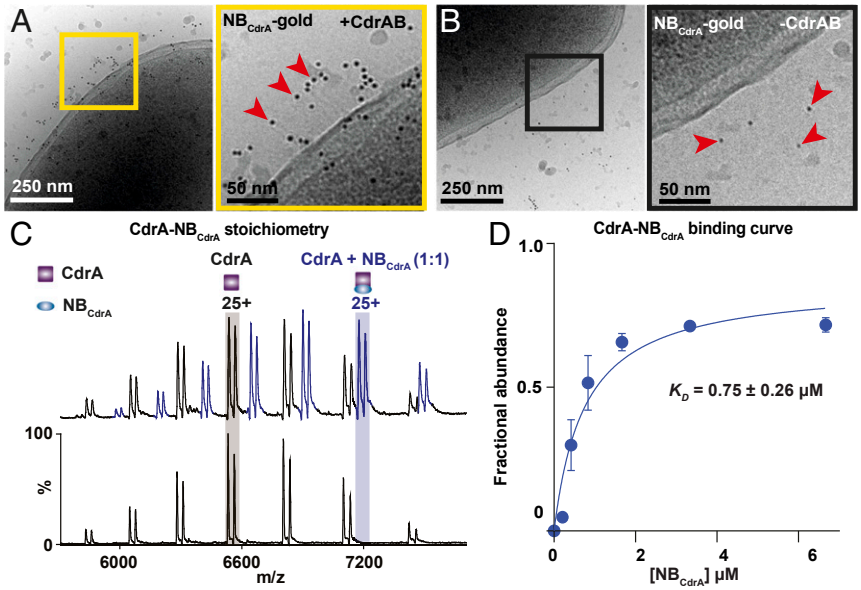

Fig. 5. Nanobody binding to CdrA on cells and in vitro. (*A* and *B*) Cryo-EM micrographs of (*A*) cells with induced CdrAB expression or (*B*) control cells, labeled with a NB_{CdrA}-gold conjugate (red arrowheads). Cropped and magnified views of the boxed areas in each panel are shown. (*C*) Native mass spectra of CdrA alone (lower spectrum) or CdrA bound to the CdrA-specific nanobody NB_{CdrA} (upper spectrum) shows binding in a 1:1 ratio. (*D*) A series of native MS experiments with increasing NB_{CdrA} concentrations were performed, yielding a binding curve. Each data point shows the relative fractional intensity of NB_{CdrA} binding peaks over total peak intensity (labeled as fractional abundance) versus NB_{CdrA} concentration. SD (error bars) was calculated from the average of five observed charge states in three independent experiments. Refer also to *SI Appendix*, Fig. S4.

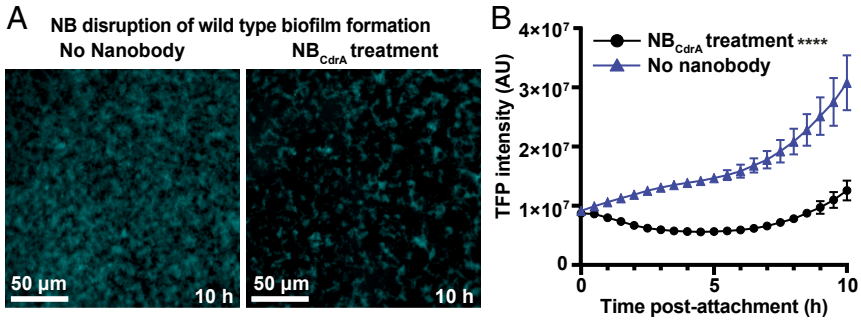

Fig. 6. Nanobody-mediated disruption of CdrA inhibits biofilm formation. (*A*) Biofilms of *P. aeruginosa* PA14 expressing TFP (teal fluorescent protein) were cultivated in the presence or absence of NB_{CdrA} and monitored over 10 h under microfluidics flow cell conditions. Representative images are shown. (*B*) Quantification of fluorescence in the experiments described in *A*. Each time point represents three images per time point from at least three independent experiments (error bars show SD). Statistical significance was assessed using the Student's *t* test at all times points (****$P < 0.0001$ at all times at or after 2.5 h post treatment). Refer also to *SI Appendix*, Fig. S5.

specimen is not needed. We next investigated whether preformed, mature *P. aeruginosa* biofilms could also be disrupted by NB_{CdrA}. Using the same flow setup, we found that bacterial cells in preformed PA14 biofilms were efficiently killed when an otherwise sublethal colistin antibiotic treatment was supplemented with NB_{CdrA} (Fig. 7 *A* and *B* and Movie S5). The efficacy of bacterial killing was substantially increased when NB_{CdrA} was added earlier, during biofilm development, before the addition of colistin (Fig. 7 *A* and *B*), in line with our data demonstrating the inhibitory effect of NB_{CdrA} on developing biofilms (Fig. 6). PAO1 biofilms were similarly susceptible to colistin-mediated bacterial killing when pretreated with NB_{CdrA}, although a higher concentration of nanobody was required to achieve a similar effect (Fig. 7*C* and *SI Appendix*, Fig. S6). These results using wild-type *P. aeruginosa* biofilms demonstrate the key role of the CdrA protein in mediating cell–cell interactions and highlight the importance of these interactions for effective biofilm formation, which directly promote tolerance of those biofilms to antibiotic treatment.

Discussion

Our results establish that functional cell-surface CdrA forms an extended structure, projecting into the EPS matrix, to mediate cell–cell interactions. This arrangement is consistent with CdrA acting as a molecular tether, in which copies of CdrA anchored on the cell surface at their C termini may be glued at their N-terminal adhesive regions by secreted polysaccharides, known to be abundant in the EPS matrix of *P. aeruginosa* and previously shown to interact with CdrA (13, 24). Our results demonstrate that CdrA is a major adhesin mediating biofilm formation in wild-type *P. aeruginosa* and show that adhesins with similar roles, such as LecB (27), cannot effectively compensate for its disruption. The difference in the sensitivity of different *P. aeruginosa* strains (PA14 and PAO1) to NB_{CdrA} treatment (Fig. 7) suggests variability in the contribution of CdrA or its accessibility during biofilm formation.

Nevertheless, while the exact contribution of different adhesins in *P. aeruginosa* biofilm development will require detailed experiments to delineate, the prominent role of CdrA-mediated cell–cell junctions is highlighted by our experiments. Our reconstituted cell flocculation system used a non–LapG-cleavable mutant of CdrA, which was important for in situ imaging using cryo-ET. Future innovative assays will be needed to replicate structural studies with wild-type CdrA protein at cell–cell junctions. The wild-type protein, natively secreted from cells, had the same overall architecture as the carboxyl-terminal non–LapG-cleavable mutant of CdrA (Fig. 2*C*). We predict that this mutation at the carboxyl-terminal membrane anchor 70 nm away from the adhesive tip of CdrA will have little or no effect on its adhesive function, as indicated by the ability of CdrA(TRRG) to form cell–cell junctions in our assays.

This paradigm of a bacterial adhesin interacting with the EPS matrix is functionally distinct from either the alternative "Velcro-like" mechanism of cell–cell adhesion proposed for *E. coli* Ag43 (18) or from the more nuanced case of *V. cholerae* in which multiple adhesins and exopolysaccharides appear to regulate cell–cell interactions (14, 16). In both *E. coli* and *V. cholerae*, the spatial organization of cell–cell junctions in biofilms has not yet been observed experimentally at high resolution, and further research will be needed to understand the arrangement of these junctions at the molecular level. In our in situ cryo-ET data, while CdrA proteins were observed, extracellular polysaccharides could not be resolved. It therefore remains to be described how polysaccharides are arranged in the EPS matrix in relation to bacterial cells and other matrix molecules. While it is possible that direct CdrA:CdrA interactions may additionally stabilize *P. aeruginosa* cell junctions in some strains (25), these were not observed in our data.

Recently, latest generation optical microscopy techniques have proven invaluable in providing novel insights into bacterial biofilm formation (14, 15, 28). In this study, we have leveraged the latest cryo-ET techniques to reveal the arrangement of cell–cell junctions that are of key importance in biofilm formation. This study highlights the utility of FIB milling and cryo-ET to deliver high-resolution insights into tissue-like multicellular specimens, which have traditionally been considered beyond the reach of structural cell biology. With increasing throughput and automation of these methods (29, 30), structure determination of molecules in cell–cell junctions may become practical and a possible extension of this work in the future.

Moreover, we also show that biofilm formation in wild-type *P. aeruginosa* bacteria can be inhibited by targeting the filamentous CdrA adhesin with a nanobody binder that interacts with the tip of the functional protein in a 1:1 ratio. Although gold-labeled nanobody was concentrated ~70 nm away from the outer membrane of *P. aeruginosa* bacteria at the tip of CdrA adhesins, identifying the exact epitope of nanobody-binding to CdrA will require higher resolution structural data. Our results are consistent with the scenario in which nanobody-binding precludes the interaction between CdrA and polysaccharides in the EPS matrix (Fig. 8). This nanobody was further shown to promote the activity of an antibiotic in killing bacterial cells in a preformed wild-type *P. aeruginosa* biofilm. The strategy of neutralizing biofilm adhesion mechanisms may also be applicable to similar large cell-surface adhesins such as the filamentous hemagglutinin of *Bordetella pertussis* (31) and the repeat-in-toxin domain-containing adhesins such as SiiE of *Salmonella enterica* and LapA from *Pseudomonas fluorescens* (32–34). Such an approach may also be useful in treating bacteria whose adhesins utilize alternative proposed cell–cell adhesion mechanisms, such as Ag43 of *E. coli* (18) or RbmA of *V. cholerae* (16).

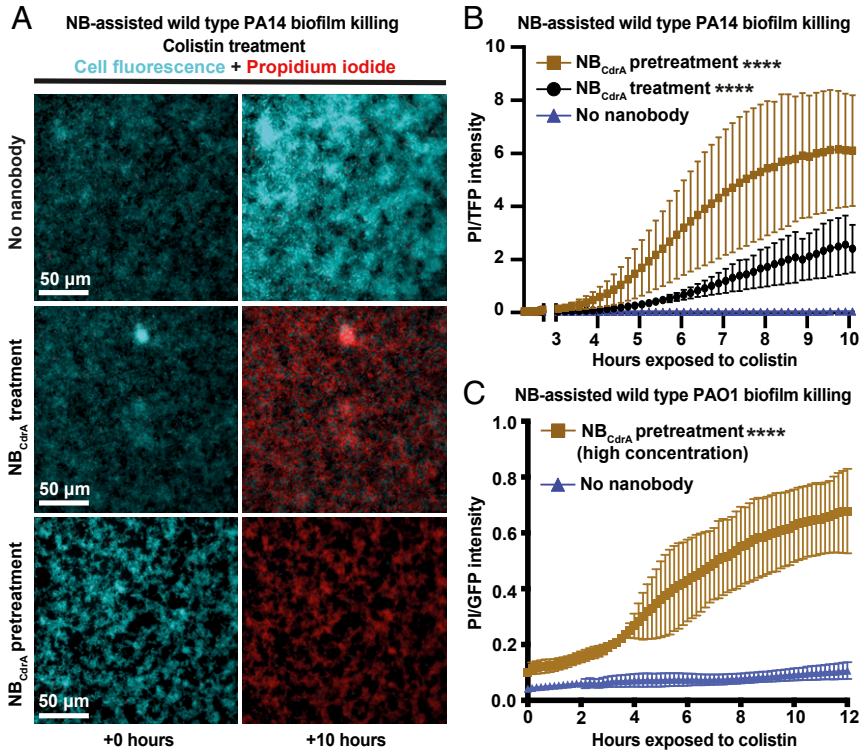

Fig. 7. Nanobody-assisted bacterial killing in preexisting, mature biofilms. (*A*) Biofilms were grown in a microfluidics flow setup either in the presence ("NB$_{CdrA}$ pretreatment") or absence ("No-nanobody" or "NB$_{CdrA}$ treatment") of NB$_{CdrA}$. After 10 h, NB$_{CdrA}$ was added to the "NB$_{CdrA}$ treatment" condition, and all samples were treated with PI (propidium iodide) and a sublethal dose of colistin (1 μg/mL) and imaged for a further ∼10 h. Fluorescence microscopy images with TFP (blue) for live cells or PI staining (red) for dead cells are shown. (*B*) Quantification of fluorescence in the experiments described in *A*, following the addition of colistin. The ratio of PI to TFP fluorescence was calculated over three replicate experiments (error bars denote SD). Statistical significance was assessed using the Student's *t* test for all time points (****$P < 0.0001$, for times after 6 to 7 h versus the no-nanobody control). (*C*) Quantification of fluorescence in the experiments performed on PAO1 strain of *P. aeruginosa*, following the addition of colistin. The ratio of PI to green fluorescent (GFP) fluorescence was calculated over three replicate experiments (error bars denote SD). Statistical significance was assessed using the Student's *t* test for all time points (****$P < 0.0001$) for times after 10 h versus the no-nanobody control). Refer to *SI Appendix*, Fig. S6 for images.

While neutralizing therapies now represent an important treatment route for many diseases, they remain relatively underexploited in the field of antimicrobials (35, 36). In the context of the increasing challenges posed by the emergence of antimicrobial resistance (37, 38), our results highlight how specific adhesins on the surface of bacterial cells may serve as promising targets for biofilm inhibition or for the prevention of chronic infections in a medical setting.

Materials and Methods

Refer also to *SI Appendix, Supplementary Text* for further details.

Cultivation of Biofilm-Like Floccules. For CdrAB(TRRG) expression, an arabinose-inducible pMQ72 plasmid system was used, as described in ref. 23, and transformed into the PAO1 Δ*pslBCD* or PAO1 Δ*cdrA* strains, described in ref. 22. The strains PAO1 Δ*psl* pMQ72-*cdrAB*(TRRG) and PAO1 Δ*cdrA* pMQ72-*cdrAB*(TRRG) were tested alongside a PAO1 Δ*cdra* pMQ72 empty vector control. Cultures were induced with arabinose to induce flocculation. To disaggregate cells, floccules were briefly vortexed with (for strains with wild-type Psl) or without (for the Psl deletion strain) the addition of 0.5% mannose (weight/volume). To stain for Psl-containing sugars, floccules were pelleted and resuspended in 80 μg/mL Alexa488-conjugated *Narcissus pseudonarcissus* lectin (Glycomatrix) for 30 min at 4 °C, washed three times with phosphate-buffered saline (PBS), and deposited on a glass slide ahead of imaging. Microscopy of floccules was performed using a Zeiss Axio Imager M2 microscope.

CdrA Protein Purification. To purify CdrA, subcultures of PAO1 Δ*pslBCD* pMQ72-*cdrAB*(TRRG) were plated on lysogeny broth agar–supplemented with gentamicin and arabinose to induce CdrAB expression and incubated overnight at 37 °C. The following day, cells were scraped from the plates into PBS, vortexed to shear CdrA from the outer membrane, and centrifuged to remove cells. The supernatant was precipitated with polyethyleneglycol 6,000 and centrifuged to remove contaminating proteins. The resulting soluble CdrA sample was dialyzed and purified by anion exchange chromatography. Eluted fractions were analyzed by sodium dodecyl sulfate–polyacrylamide gel eletrophoresis

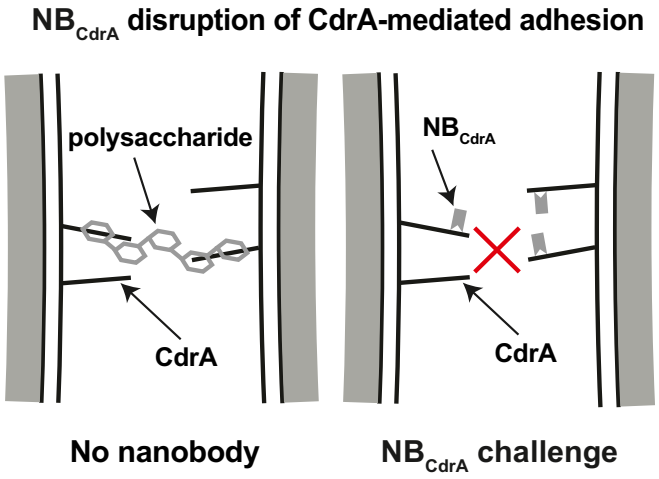

Fig. 8. CdrA-mediated cell–cell junctions. Schematic depiction of the mechanism of biofilm inhibition by targeting CdrA revealed in this study. Refer also to Movie S5.

(SDS-PAGE), and fractions containing CdrA were further purified by size exclusion chromatography.

Nanobody Generation. Antibodies to CdrA were raised in a llama by intramuscular immunization with purified protein using Gerbu LQ#3000 as the adjuvant. Total RNA was extracted from blood, and VHH complementary DNAs were generated by RT-PCR. The pool of VHH-encoding sequences was amplified by two rounds of nested PCR and cloned into the SfiI sites of the phagemid vector pADL-23c. Electro-competent *E. coli* TG1 cells were transformed with the recombinant pAD-23c vector, and the resulting TG1 library stock was infected with M13K07 helper phage to obtain a library of VHH-presenting phages. Phages displaying VHHs specific for CdrA were enriched via two rounds of bio-panning on biotinylated CdrA, and individual phagemid clones were picked. VHH-displaying phages were recovered by infection with M13K07 helper phage and tested for binding to CdrA by enzyme-linked immunosorbent assay (ELISA). Phage binders were ranked according to the ELISA signal and grouped according to CDR3 sequence identity.

Nanobody Expression and Purification. To express nanobodies, nanobody phagemids were first transformed by heat shock into WK6 *E. coli* cells. Subcultures of transformants were prepared and induced with isopropyl β-D-thiogalactoside and incubated overnight. The following day, cells were pelleted, resuspended in a lysing buffer, and homogenized. His-tagged nanobodies were purified by Ni-NTA affinity chromatography and size exclusion chromatography.

Native MS of CdrA and Nanobodies. Data were collected on a Q-Exactive ultrahigh mass range mass spectrometer (Thermo Fisher Scientific) and analyzed using Xcalibur 4.2 (Thermo Fisher Scientific) and UniDec (39) software packages. Nanobody-binding experiments were performed by adding increasing amounts of NB_{CdrA} to a constant 2 μM CdrA. The resulting calculated binding affinity (K_D) from native MS was determined by employing a nonlinear regression curve fitting for one-site specific binding in GraphPad Prism 8.0.

Protein Identification by Proteomics. For protein identification, tryptic peptides were obtained by digesting the protein sample with trypsin as described in ref. 40. Peptides separated using a chromatographic system connected to an Eclipse Tribrid Orbitrap mass spectrometer (Thermo Fisher Scientific). Raw data files were processed for protein identification using MaxQuant (version 1.6.3.4) and searched against the UniProt database.

Nanobody Gold Conjugation and Labeling. NB_{CdrA} was dialyzed into 20 mM Tris pH 7.4, 150 mM NaCl, and incubated with a ∼2.5× molar excess of Ni-NTA 5-nm gold (Nanoprobes) for 30 min at room temperature. Unbound gold was separated from NB_{CdrA}-gold using a PD-10 desalting column. To label cells, NB_{CdrA}-gold was incubated with PAO1 Δ*cdrA* pMQ72-*cdrAB*(TRRG) floccules followed by the addition of mannose ahead of cryo-EM sample preparation.

Nanobody-Mediated Batch Biofilm Disruption Assays. To assess the efficacy of nanobody-mediated floccule disaggregation, PAO1 Δ*cdrA* pMQ72-*cdrAB*(TRRG) bacterial floccules were incubated with NB_{CdrA} or $NB_{CdrA\text{-}2}$. Floccules were pelleted at 300 × *g* for 5 min. The supernatant was removed, and the remaining cells were pelleted at 15,000 × *g* for 15 min. The two pelleted fractions were weighed, and floccule mass was calculated as a percentage of total cell mass.

Microfluidics-Based Microscopy and Analysis. To determine the effect of nanobodies on the formation of wild-type biofilms, a previously described flow system was used (41). *P. aeruginosa* PA14 or PAO1 was visualized via fluorescence of the teal fluorescent protein (TFP) or green fluorescent protein (GFP), respectively. Biofilms were grown and visualized in microfluidics chambers generated through soft lithography techniques (42, 43). Bacteria were prepared as described previously (44). Bacterial cultures were allowed to attach for 1 h without flow, after which the flow rate was set to 1.0 μL/min and imaged for 10 to 12 h, as indicated.

For the biofilm inhibition assays, the biofilm medium was supplemented either with no-nanobody, 0.3 mg/mL NB_{CdrA} (PA14 cells), or 0.8 mg/mL NB_{CdrA} (PAO1 cells) as indicated and imaged for ∼10 h postinoculation. To test the impact of colistin on a preformed biofilm, bacteria were prepared, inoculated, and grown in microfluidics chambers as described above. After 10 h of allowing the biofilm to establish in the absence of any treatment, KA medium was switched with KA medium supplemented with propidium iodide (PI) and 1.0 μg/mL colistin $^{+/-}$ NB_{CdrA}, as indicated and imaged for an additional ∼10 h of incubation.

Sample Preparation for Cryo-EM. Cryo-EM samples were prepared by depositing 2.5 μL of bacterial floccules, disaggregated bacterial floccules (single cells), or NB_{CdrA}-gold–labeled cells onto freshly glow discharged Quantifoil grids. Samples were fixed with 1% paraformaldehyde applied directly on the grid and manually blotted. Next, buffered fiducial gold was added, and the grid was blotted and plunge-frozen into liquid ethane using a Vitrobot Mark IV (Thermo Fisher Scientific).

Cryo-FIB Milling and Scanning Electron Microscopy. Cryo-FIB milling of plunge-frozen biofilm-like floccules was performed as described previously (45) on a Scios DualBeam FIB/scanning electron microscope (SEM) microscope (FEI/Thermo Fisher Scientific) equipped with a Quorum PP3010T cryo-FIB/SEM preparation system. The loading stage and milling procedure were adapted, with minor alterations, from ref. 46. Grids were sputter-coated with platinum before milling and coated with a layer of organometallic platinum. Ion beam current for milling was reduced stepwise while adjusting the stage tilt as described in ref. 45. Final polishing of the lamellae resulted in 150- to 300-nm-thick lamellae.

Transmission Cryo-EM and Cryo-ET. Tilt series data were collected on a Titan Krios microscope (Thermo Fisher Scientific) operating at 300 kV fitted with a Quantum energy filter (Gatan) and direct electron detector (Gatan) using SerialEM software (47). A dose-symmetric tilt scheme was employed for cryo-ET data (48). Untilted video frame stacks of purified protein were collected on the same microscope using EPU software (Themo Fisher Scientific). Cryo-EM images of NB_{CdrA}-gold–labeled cells were collected on a Talos Arctica 200 kV cryo-ET (Thermo Fisher Scientific).

Tilt series alignment was carried out using the eTOMO graphical user interface in the IMOD software (47). CTF (contrast transfer function) parameters for the aligned stacks were estimated using CTFFIND (49), and data were reconstructed using Tomo3D (50). Contrast in cryo-ET data were enhanced via the tom_deconv deconvolution as described in ref. 51 or via bandpass and Laplacian filtering as implemented in Fiji (52). Segmentation of image data were performed manually in IMOD (47).

Data Availability. All study data are included in the article and/or supporting information.

ACKNOWLEDGMENTS. T.A.M.B. is a recipient of a Sir Henry Dale Fellowship, jointly funded by the Wellcome Trust and the Royal Society (202231/Z/16/Z). T.A.M.B. thanks the Vallee Research Foundation and the John Fell Fund for support. G.A.O. acknowledges support from the NIH (R37-AI83256), and C.V.R. acknowledges funding from the Medical Research Council (MR/N020413/1). J.H. is funded by the Edward Penley Abraham Cephalosporin Fund, and Protein Production United Kingdom is supported by the Rosalind Franklin Institute Engineering and Physical Sciences Research Council Grant EP/S025243/1. We thank Adam Costin for help with cryo-EM imaging, Carey Nadell for providing the microfluidics chambers, and Wanda Kukulski for facilitating FIB milling experiments. We would like to acknowledge the MRC Laboratory of Molecular Biology Electron Microscopy Facility for access to cryo-FIB sample preparation.

1. H. C. Flemming, S. Wuertz, Bacteria and archaea on Earth and their abundance in biofilms. *Nat. Rev. Microbiol.* **17**, 247–260 (2019).
2. L. Hall-Stoodley, J. W. Costerton, P. Stoodley, Bacterial biofilms: From the natural environment to infectious diseases. *Nat. Rev. Microbiol.* **2**, 95–108 (2004).
3. J. W. Costerton *et al*., Bacterial biofilms in nature and disease. *Annu. Rev. Microbiol.* **41**, 435–464 (1987).
4. Y. Fan, O. Pedersen, Gut microbiota in human metabolic health and disease. *Nat. Rev. Microbiol.* **19**, 55–71 (2020).
5. H. L. P. Tytgat, F. L. Nobrega, J. van der Oost, W. M. de Vos, Bowel biofilms: Tipping points between a healthy and compromised gut? *Trends Microbiol.* **27**, 17–25 (2019).
6. M. Kostakioti, M. Hadjifrangiskou, S. J. Hultgren, Bacterial biofilms: Development, dispersal, and therapeutic strategies in the dawn of the postantibiotic era. *Cold Spring Harb. Perspect. Med.* **3**, a010306 (2013).
7. G. A. O'Toole, G. C. L. Wong, Sensational biofilms: Surface sensing in bacteria. *Curr. Opin. Microbiol.* **30**, 139–146 (2016).
8. H. C. Flemming *et al*., Biofilms: An emergent form of bacterial life. *Nat. Rev. Microbiol.* **14**, 563–575 (2016).
9. L. Hall-Stoodley, P. Stoodley, Evolving concepts in biofilm infections. *Cell. Microbiol.* **11**, 1034–1043 (2009).
10. C. W. Hall, T. F. Mah, Molecular mechanisms of biofilm-based antibiotic resistance and tolerance in pathogenic bacteria. *FEMS Microbiol. Rev.* **41**, 276–301 (2017).

11. C. Matz, S. Kjelleberg, Off the hook – How bacteria survive protozoan grazing. *Trends Microbiol.* **13**, 302–307 (2005).
12. J. S. Gunn, L. O. Bakaletz, D. J. Wozniak, What's on the outside matters: The role of the extracellular polymeric substance of gram-negative biofilms in evading host immunity and as a target for therapeutic intervention. *J. Biol. Chem.* **291**, 12538–12546 (2016).
13. H. C. Flemming, J. Wingender, The biofilm matrix. *Nat. Rev. Microbiol.* **8**, 623–633 (2010).
14. V. Berk *et al*., Molecular architecture and assembly principles of *Vibrio cholerae* biofilms. *Science* **337**, 236–239 (2012).
15. K. Drescher *et al*., Architectural transitions in *Vibrio cholerae* biofilms at single-cell resolution. *Proc. Natl. Acad. Sci. U.S.A.* **113**, E2066–E2072 (2016).
16. J. C. Fong *et al*., Structural dynamics of RbmA governs plasticity of *Vibrio cholerae* biofilms. *eLife* **6**, e26163 (2017).
17. M. Maestre-Reyna, W. J. Wu, A. H. Wang, Structural insights into RbmA, a biofilm scaffolding protein of *V. cholerae*. *PLoS One* **8**, e82458 (2013).
18. B. Heras *et al*., The antigen 43 structure reveals a molecular Velcro-like mechanism of autotransporter-mediated bacterial clumping. *Proc. Natl. Acad. Sci. U.S.A.* **111**, 457–462 (2014).
19. S. T. Clark, D. S. Guttman, D. M. Hwang, Diversification of *Pseudomonas aeruginosa* within the cystic fibrosis lung and its effects on antibiotic resistance. *FEMS Microbiol. Lett.*, 10.1093/femsle/fny026 (2018).
20. A. K. Tarafder *et al*., Phage liquid crystalline droplets form occlusive sheaths that encapsulate and protect infectious rod-shaped bacteria. *Proc. Natl. Acad. Sci. U.S.A.* **117**, 4724–4731 (2020).
21. J. M. Sweere *et al*., Bacteriophage trigger antiviral immunity and prevent clearance of bacterial infection. *Science* **363**, eaat9691 (2019).
22. B. R. Borlee *et al*., *Pseudomonas aeruginosa* uses a cyclic-di-GMP-regulated adhesin to reinforce the biofilm extracellular matrix. *Mol. Microbiol.* **75**, 827–842 (2010).
23. R. B. Cooley *et al*., Cyclic Di-GMP-regulated periplasmic proteolysis of a *Pseudomonas aeruginosa* type Vb secretion system substrate. *J. Bacteriol.* **198**, 66–76 (2015).
24. C. Reichhardt *et al*., The versatile *Pseudomonas aeruginosa* biofilm matrix protein CdrA promotes aggregation through different extracellular EPS interactions. *J. Bacteriol.* **202**, e00216–e00220 (2020).
25. C. Reichhardt, C. Wong, D. Passos da Silva, D. J. Wozniak, M. R. Parsek, CdrA interactions within the *Pseudomonas aeruginosa* biofilm matrix safeguard it from proteolysis and promote cellular packing. *mBio* **9**, e01376–e18 (2018).
26. T. Uchański, E. Pardon, J. Steyaert, Nanobodies to study protein conformational states. *Curr. Opin. Struct. Biol.* **60**, 117–123 (2020).
27. D. Passos da Silva *et al*., The *Pseudomonas aeruginosa* lectin LecB binds to the exopolysaccharide Psl and stabilizes the biofilm matrix. *Nat. Commun.* **10**, 2183 (2019).
28. B. Qin *et al*., Cell position fates and collective fountain flow in bacterial biofilms revealed by light-sheet microscopy. *Science* **369**, 71–77 (2020).
29. J. Böhning, T. A. M. Bharat, Towards high-throughput in situ structural biology using electron cryotomography. *Prog. Biophys. Mol. Biol.* **160**, 97–103 (2020).
30. G. L. Weiss, A. K. Kieninger, I. Maldener, K. Forchhammer, M. Pilhofer, Structure and function of a bacterial gap junction analog. *Cell* **178**, 374–384.e15 (2019).
31. J. A. Melvin, E. V. Scheller, J. F. Miller, P. A. Cotter, *Bordetella pertussis* pathogenesis: Current and future challenges. *Nat. Rev. Microbiol.* **12**, 274–288 (2014).
32. B. Peters *et al*., Structural and functional dissection reveals distinct roles of Ca^{2+}-binding sites in the giant adhesin SiiE of *Salmonella enterica*. *PLoS Pathog.* **13**, e1006418 (2017).
33. T. J. Smith, M. E. Font, C. M. Kelly, H. Sondermann, G. A. O'Toole, An N-terminal retention module anchors the giant adhesin LapA of *Pseudomonas fluorescens* at the cell surface: A novel subfamily of type I secretion systems. *J. Bacteriol.* **200**, e00734–e17 (2018).
34. S. Guo, T. D. R. Vance, C. A. Stevens, I. K. Voets, P. L. Davies, RTX adhesins are key bacterial surface megaproteins in the formation of biofilms. *Trends Microbiol.* **27**, 470 (2019).
35. L. L. Burrows, The therapeutic pipeline for *Pseudomonas aeruginosa* infections. *ACS Infect. Dis.* **4**, 1041–1047 (2018).
36. E. Pelfrene, M. Mura, A. Cavaleiro Sanches, M. Cavaleri, Monoclonal antibodies as anti-infective products: A promising future? *Clin. Microbiol. Infect.* **25**, 60–64 (2019).
37. R. C. MacLean, A. San Millan, The evolution of antibiotic resistance. *Science* **365**, 1082–1083 (2019).
38. C. Nathan, Resisting antimicrobial resistance. *Nat. Rev. Microbiol.* **18**, 259–260 (2020).
39. M. T. Marty *et al*., Bayesian deconvolution of mass and ion mobility spectra: From binary interactions to polydisperse ensembles. *Anal. Chem.* **87**, 4370–4376 (2015).
40. A. Shevchenko, M. Wilm, O. Vorm, M. Mann, Mass spectrometric sequencing of proteins silver-stained polyacrylamide gels. *Anal. Chem.* **68**, 850–858 (1996).
41. C. Sternberg, T. Tolker-Nielsen, Growing and analyzing biofilms in flow cells. *Curr. Protoc. Microbiol.*, 10.1002/9780471729259.mc01b02s00 (2006).
42. S. K. Sia, G. M. Whitesides, Microfluidic devices fabricated in poly(dimethylsiloxane) for biological studies. *Electrophoresis* **24**, 3563–3576 (2003).
43. D. B. Weibel, W. R. Diluzio, G. M. Whitesides, Microfabrication meets microbiology. *Nat. Rev. Microbiol.* **5**, 209–218 (2007).
44. A. J. Collins, A. B. Pastora, T. J. Smith, G. A. O'Toole, A. Map, MapA, a second large RTX adhesin conserved across the pseudomonads, contributes to biofilm formation by *Pseudomonas fluorescens*. *J. Bacteriol.* **202**, e00277–e20 (2020).
45. P. C. Hoffmann *et al*., Tricalbins contribute to cellular lipid flux and form curved ER-PM contacts that are bridged by rod-shaped structures. *Dev. Cell* **51**, 488–502.e8 (2019).
46. M. Schaffer *et al*., Cryo-focused ion beam sample preparation for imaging vitreous cells by cryo-electron tomography. *Bio Protoc.* **5**, e1575 (2015).
47. D. N. Mastronarde, Automated electron microscope tomography using robust prediction of specimen movements. *J. Struct. Biol.* **152**, 36–51 (2005).
48. W. J. H. Hagen, W. Wan, J. A. G. Briggs, Implementation of a cryo-electron tomography tilt-scheme optimized for high resolution subtomogram averaging. *J. Struct. Biol.* **197**, 191–198 (2017).
49. A. Rohou, N. Grigorieff, CTFFIND4: Fast and accurate defocus estimation from electron micrographs. *J. Struct. Biol.* **192**, 216–221 (2015).
50. J. J. Fernandez, S. Li, T. A. M. Bharat, D. A. Agard, Cryo-tomography tilt-series alignment with consideration of the beam-induced sample motion. *J. Struct. Biol.* **202**, 200–209 (2018).
51. D. Tegunov, P. Cramer, Real-time cryo-electron microscopy data preprocessing with Warp. *Nat. Methods* **16**, 1146–1152 (2019).
52. J. Schindelin *et al*., Fiji: An open-source platform for biological-image analysis. *Nat. Methods* **9**, 676–682 (2012).